Ultrasensitive graphene far-infrared power detectors

IOP Publishing Journal of Physics: Condensed Matter
J. Phys.: Condens. Matter **27** (2015) 164203 (13pp) doi:10.1088/0953-8984/27/16/164203

Ultrasensitive graphene far-infrared power detectors

C B McKitterick[1,2], D E Prober[1,2], H Vora[3] and X Du[3]

[1] Department of Physics, Yale University, New Haven, CT 06520, USA
[2] Department of Applied Physics, Yale University, New Haven, CT 06520, USA
[3] Department of Physics, Stony Brook University, Stony Brook, NY 11790, USA

E-mail: daniel.prober@yale.edu

Received 8 January 2015, revised 23 February 2015
Accepted for publication 25 February 2015
Published 2 April 2015

Abstract

We describe the properties of ultrasensitive graphene photon detectors for use in the far-infrared/terahertz spectral region and present theoretical predictions for their power detection sensitivity. These predictions are based on two graphene contacting schemes with superconducting contacts: contacts with a thin insulating barrier, and direct superconducting contacts. To quantitatively assess these predictions, we perform thermal measurements of graphene at low temperatures and analyse them to extract information on electron–phonon cooling in graphene. These new results for the electron–phonon cooling channel allow reliable prediction of the noise equivalent power (NEP) that can be expected from an optimized graphene detector, using measurement of the Johnson noise emission as the thermometry method. We find that an NEP of 2×10^{-19} W Hz$^{-1/2}$ should be achievable under certain biasing conditions with an ideal device.

Keywords: far-infrared, terahertz, photodetector, NEP, Johnson noise, graphene

(Some figures may appear in colour only in the online journal)

1. Introduction

Graphene—the two-dimensional form of graphite, has provided new opportunities for novel devices and for fundamental physics studies. With its small number of conduction electrons ($n \sim 10^{10}$–10^{13} cm^{-2}), graphene has been explored as a sensitive detector of photons from millimetre/far-infrared wavelengths through the visible region of the spectrum. The detection mechanisms and important areas of application vary with the wavelength being considered. Visible/near-IR photon detection has been explored in theory and in experiment [1–5]. Detection in the far-IR/ THz region (referred to below as THz region) has been studied at relatively large power [6–10] and previous studies have provided theoretical predictions for low power [11–17].

The focus of this paper is the detection of THz/far-IR photons at extremely low power, requiring the highest sensitivity. Potential applications include space-based astronomy observations and solid-state physics studies at very low temperatures [18–20]. The mechanisms of very sensitive THz detection differ from those for near-IR and visible photons and for large THz power, where photo-electrothermal effects can be employed effectively. At low excitation energies and temperatures $T < 1$ K, which are necessary to achieve the required sensitivity, the electrothermal coefficients become very small. Thus, we investigate ultrasensitive THz detection at low temperatures by using the heating of a graphene electron system from incident THz radiation, and detection of the resulting temperature rise. The temperature rise can be detected using the change in emitted Johnson noise, or the change of the resistance of superconducting (SC) tunnel barrier contacts.

In this paper we outline the main requirements and constraints for an ultrasensitive graphene thermal photodetector in the THz spectral region. We describe our experiments that characterize graphene devices with metallic direct contacts. In addition, we describe the expected device performance with SC tunnel contacts. The readout mechanisms that can be used with these contacts include a resistive readout (for tunnel contacts only) and a Johnson noise readout. We also describe our recent experiments that determine the strength of the electron–phonon coupling, which controls the thermal conductance and the ultimate detector sensitivity. With these data we predict the expected performance as a THz power detector.

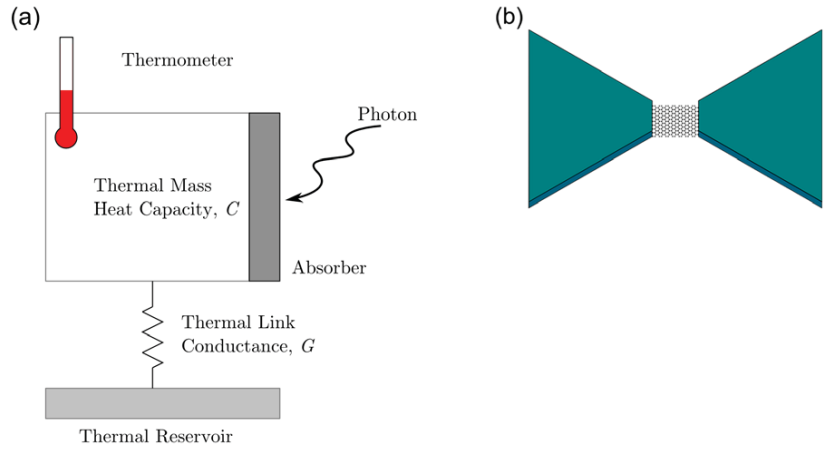

Figure 1. Schematic of the thermal photon detection process (*a*) and antenna coupled graphene device (*b*). To couple efficiently to THz photons, the antenna's linear dimensions will need to be ∼100 μm.

1.1. Device physics

For ultrasensitive detection in the THz/far-IR region, operation at low temperature ($\leqslant$1 K) is essential. Here we develop the engineering and sensitivity requirements for a graphene detector and treat the physics requirements and constraints. With very low average power, as envisioned in the astronomy applications (e.g. $P = 0.1$–100 aW), the arrival rate of THz photons is approximately 10^2–10^5 s^{-1}. In this paper we treat the issues of measuring single THz photons and of measuring the power of a very weak incident photon flux. Single photon counting with graphene has been treated in recent papers [11–15], and might be employed, but only if graphene had the extremely small thermal conductance below 1 K which has been extrapolated in a previous study [21]. Our recent experiments, and most others described later, find a much larger extrapolated thermal conductance. This larger thermal conductance leads to a diminished device performance as shown in section 4. We consider the use of graphene to measure the average power over a time (on the order of 1 s). This has relaxed sensitivity requirements compared to single-photon counting. We find that the graphene device does show promise for this mode of power detection.

The design considerations for the graphene electron physics follow from the above specifications. The dominant absorption mechanism for the anticipated electron densities is Drude absorption for frequencies up to a few THz [22]. With a device resistance that matches the impedance of the antenna (see figure 1), full absorption can occur. This contrasts with the much weaker absorption of monolayer graphene at mid-IR wavelengths, $\leqslant$2% [23]. We consider the response to individual photons, since the arrival rate ($\leqslant 10^5$ s^{-1}) is less than the inverse decay time (10^6 s^{-1}). An absorbed THz photon initially creates one excited internal photoelectron, which rapidly shares its energy with the other electrons to produce an elevated initial electron temperature $T_\mathrm{i} = T_0 + \Delta T_\mathrm{i}$; T_0 is the base (quiescent) temperature. We describe this process with the simple model of figure 1. The initial electron–electron sharing of the energy is quite rapid [24–26], and occurs more rapidly than phonon emission. The subsequent decay from T_i back towards T_0 is slower, on the order of 1 μs. We first treat the simplest case: the nearly linear regime where $\Delta T_i < T_0$. If all the photon energy goes into electron thermal excitations, then

$$\Delta T_\mathrm{i} = E/C, \tag{1.1}$$

With E the photon energy ($E \approx 7 \times 10^{-22}$ J for 1 THz) and C the heat capacity of the graphene, which is proportional to the graphene area.

After photon absorption, the excess temperature decays as $\Delta T\ (t) = \Delta T_\mathrm{i} \mathrm{e}^{-t/\tau}$ with a thermal relaxation time

$$\tau = \frac{C}{G}. \tag{1.2}$$

G is the total thermal conductance seen by the graphene electron system [27]. The thermal relaxation time is the signal averaging time for single photon detection. In section 4.2, we predict that, for devices which remain approximately linear in device response, $\tau \approx 2.5$ μs at 50 mK. A longer relaxation time allows for the readout noise to be reduced through averaging, discussed in detail in sections 2.1 and 2.2. We will show there that a long relaxation time, and thus a small thermal conductance, is desirable to reduce the noise in the detector for both single-photon and power detection. The total thermal conductance arises from three cooling pathways. The electron system can relax back to the equilibrium temperature by the warm electrons (1) emitting phonons into the graphene (G_eph), (2) diffusing out the leads (G_diff), and (3) emitting blackbody radiation into the microwave environment (G_photon). These conductances are parallel channels and add linearly to give the total thermal conductance:

$$G = G_\mathrm{eph} + G_\mathrm{diff} + G_\mathrm{photon}. \tag{1.3}$$

There are two detection modes that we consider in this paper: single-photon detection and power detection. A longer averaging time is used to measure the power of the incident photon flux. For this second application of measuring an incident power P, the time-average temperature rise is given by

$$\Delta T = P/G, \tag{1.4}$$

where we again assume that $\Delta T < T_i$ and G is the total thermal conductance given above. For both single-photon detection and for power measurements, a smaller value of G increases the sensitivity of the detector. If the electrical contacts are a non-SC metal then $G_{\rm diff} \gg G_{\rm eph}, G_{\rm photon}$ at the low temperatures necessary for the detection of THz photons. Thus, to retain the photon energy in the graphene electron system, $G_{\rm diff}$ should be minimized. A strategy that can make $G_{\rm diff}$ small for the heated electron system is to employ SC contacts [28]. The energy gap Δ of the SC contacts should be $\Delta \gg k_{\rm B}T$ so the electrons which are excited due to the absorbed photon energy will be strongly confined to the graphene [28], to slowly leak out via phonon or photon emission.

We discuss below experiments on graphene with two kinds of contacts to the SC wiring: (1) tunnelling contacts using a thin insulating layer, denoted SIN and (2) metallic direct contacts to the graphene, denoted SN. S is the superconductor, I the thin insulator (if present), and N the non-SC graphene. For SIN contacts, the low-frequency electrical resistance $R(T)$ is large and depends exponentially on $\Delta/k_{\rm B}T$ at low bias voltage [28]. Measurement of the resistance change provides a convenient measure of the electron temperature change following photon absorption. On the other hand, we also consider the fact that the large dc resistance may cause a long electrical RC response time, due to the presence of parasitic capacitance (e.g. from the wiring and from other circuit components such as amplifiers). This can preclude single-photon detection if this electrical response time is longer than the time interval between photon absorption events. In addition, $R(T)$ is strongly dependent on temperature; this limits the range of incident power for which the response is linear for power measurements.

SN contacts have low electrical resistance, but still give confinement of the heat in the graphene due to Andreev reflection [28]. Andreev reflection occurs at a clean interface between a superconductor with energy gap Δ and a normal metal (non-superconductor). At low energies ($eV \ll \Delta$) transmission of charge from the normal metal to the superconductor can only happen if a pair of electrons, a Cooper pair, is created in the superconductor. That can occur via the Andreev reflection process [28] where a an electron excitation incident on the interface results in a hole excitation which is retro-reflected from the interface back into the normal metal. This transfers a charge of $2e$ since the hole acts like a positive charge, but this process leaves an excitation in the normal metal. Thus, the entropy of the normal metal is not reduced by this process; heat which appears as electron and hole excitations does not leave the normal metal. Andreev reflection for a graphene-superconductor interface differs in some aspects [29], but the essential reasons for heat confinement in the graphene are the same.

We require that the spacing between the SC contacts be large enough that no Josephson pair current develops. If a Josephson current were present, a finite bias current would be required to develop a finite output voltage. The resulting power dissipation would be excessive [30]. For the SN contact we can employ a Johnson-noise thermometry (JNT) readout, discussed below. This JNT readout has potential for microwave multiplexing of multiple pixels [12]. The JNT readout can also be used with the SIN contact, if the junction electrical capacitance is large enough to allow efficient coupling out of the emitted Johnson noise.

A contacting method which could be employed, but has not been studied for graphene, is the use of an insulating (non-tunnelling) contact which has sufficient electrical capacitance to couple in the THz photons efficiently [31], and to couple out the microwave Johnson noise emission. The Johnson noise readout does not require a dc connection, nor dc bias current. The choice of preferred contact, SIN, SN, or capacitive, will be determined by the feasibility of fabrication, readout amplifier, and methods of multiplexing many pixels of graphene detectors.

In this review we will describe the methods of detection for a detector with SN contacts using JNT and a detector with SIN contacts using the resistance of the tunnel barrier contacts to measure electron temperature. We will demonstrate that both methods depend critically on having a small value of $G_{\rm eph}$. The electron–phonon thermal conductance is determined by the deformation potential D, an intrinsic parameter of graphene. Our present measurements determine the value of $G_{\rm eph}$ and thus the deformation potential. Using these measurements, we will present predictions of device performance for both measurement schemes.

2. Detector operation

For ultrasensitive detection of THz photons, it is desirable to operate at low temperatures ($\leqslant$ 1 K). At these temperatures, graphene's electrical resistance is insensitive to temperature changes [32]. We discuss two distinct thermometry methods for measuring the electron temperature and their implications for device sensitivity. The first we will consider measures the emitted Johnson noise of the device to determine the electron temperature. The Johnson noise is the blackbody power emitted from the device. The power emitted into an impedance-matched load is given by the one-dimensional blackbody formula,

$$P_{\rm J} = \int_{f_1}^{f_2} \frac{hf}{{\rm e}^{\frac{hf}{k_{\rm B}T}} - 1} {\rm d}f. \tag{2.1}$$

Here $B = f_2 - f_1$ is the measurement bandwidth and T is the temperature of the electron system. We assume that the noise is coupled out only in this band B. For frequencies and temperatures where $hf \ll k_{\rm B}T$, (2.1) has the limiting form $P_{\rm J} = k_{\rm B}BT$, and is a simple linear function of temperature. We may therefore use the measured power $P_{\rm J}$ as a thermometer for the electron system.

Alternatively, SC tunnel junction contacts on the graphene yield a dc resistance that is strongly temperature dependent [28]. In such tunnelling junctions, the electrical conductance, $1/R(T)$, depends on the tunnelling probability of the thermally excited charge carriers in the graphene through the tunnel barrier into the superconductor contacts. Only those electrons in the graphene with energy $E > \Delta$ can tunnel; Δ is the SC energy gap of the contacts. As a result, for an ideal SIN tunnel junction, the tunnelling resistance at a dc voltage

$|V| \ll k_B T/e$ is given by $R(T) = R_0 \exp(\Delta/k_B T)$, where R_0 is the normal state (above T_c) tunneling resistance. With SIN contacts, the sharp change in device resistance as a function of temperature can serve as a thermometer for the graphene electron temperature. A bias current or voltage is required, as discussed in section 2.2.

2.1. Johnson noise thermometry

Accurately measuring the device temperature using a Johnson-noise thermometer requires consideration of many parameters. Optimal performance will be achieved only through careful choice of device size, measurement readout frequency, and measurement bandwidth. We treated these considerations carefully for single-photon detection in a previous study [11], so we discuss them here only briefly. In this discussion, there are two sources of noise that we focus on: intrinsic energy fluctuations of the device, and apparent temperature fluctuations due to inaccuracy in measuring the emitted microwave power to determine the temperature. Exchange of phonons and photons between the graphene and the bath lead to effective rms device temperature fluctuations in a time τ given by [33]

$$\delta T_{\rm intr} = \sqrt{k_B T_0^2 / C\,(T_0)}, \tag{2.2}$$

when the device is in equilibrium at a temperature T_0. In this expression, T_0 is the quiescent temperature of the device (the bath temperature) and $C(T) = \gamma A T$ is the graphene heat capacity; γ is the specific heat coefficient [34] and A is the device area. The readout noise is determined by the amplifier noise temperature T_A, the measurement bandwidth B, and the detection time τ (the thermal relaxation time if considering single photon detection) [11] and is given by the Dicke radiometer formula [35]:

$$\delta T_{\rm readout} = \frac{T_A + T_0}{\sqrt{B\tau}}. \tag{2.3}$$

These root-mean-square (rms) temperature uncertainties add in quadrature to yield the total temperature uncertainty $\delta T^2 = \delta T_{\rm intr}^2 + \delta T_{\rm readout}^2$. For a graphene detector to effectively detect individual THz photons, the temperature increase $\Delta T_i = T_i - T_0$ of the electron system just after photon absorption must be substantially greater than the total temperature uncertainty δT. The temperature following the absorption of a photon with energy E is given in general by

$$E = \gamma A (T_i^2 - T_0^2). \tag{2.4}$$

For the linear regime, this reduces to (1.1). This linear regime applies for photon energies which give a temperature change $\Delta T_i \ll T_0$; in that regime $C = C\,(T_0) \equiv C_0$.

To understand the important parameters when predicting the device performance, we consider the dynamics of the electron response after a photon is absorbed by the graphene detector. For single photon detection, we wish to achieve a large ratio $\Delta T/\delta T_{\rm intr}$ and $\Delta T/\delta T_{\rm intr} \propto \sqrt{1/C_0}$ for small photon energy in the linear regime. Thus, the heat capacity $C(T_0)$ of the graphene must be small to allow resolution of the individual photon response. However, for a very small C_0, the absorption of a photon will raise the temperature of the electron system T substantially above its equilibrium value T_0, so that the system no longer behaves linearly and $\Delta T_i \geqslant T_0$. The fluctuation properties of the system in the non-linear range can no longer be determined from the equilibrium predictions, as $T_i \gg T_0$. To account for this, we modelled the relaxation of the graphene temperature immediately following the absorption of a photon for the non-linear temperature response. We determined $T(t)$ and the average temperature $T_{\rm avg}$ of the graphene during the detection time τ [11]. This average temperature was then used to determine the fluctuation properties of the device during the detection time. The predictions of this approach have been presented in detail in McKitterick *et al* [11]. The total temperature uncertainty during time τ is predominantly due to the apparent temperature fluctuations of the readout system, (2.3) with $T_{\rm avg}$ substituted for T_0. Thus, choosing device parameters to maximize the product of bandwidth and relaxation time, as well as choosing a suitable amplifier to reduce the readout noise, are critical to implementing this detection scheme effectively.

Even with optimum choice of the device parameters, there is an upper limit on the magnitude of electron–phonon coupling strength for which individual photon absorption events can be resolved. If G is too large the temperature decays very rapidly as τ in (2.3) is very short. In that case, $\delta T_{\rm readout} \geqslant \Delta T_i$ and the individual photon response cannot be resolved. The diffusion thermal conductance $G_{\rm diff}$ can be suppressed with SC contacts as discussed in section 1.1, but $G_{\rm eph}$ always contributes to G. The electron–phonon thermal conductance is determined by the fundamental physics of the graphene. In metals, at low temperatures, the cooling power of the electron system through phonon emission is typically given by $P_{\rm eph} = V\Sigma\left(T^p - T_0^p\right)$, where V is the device volume, Σ is a constant which gives the strength of electron phonon coupling and p ranges from 3 to 6 [36, 37]. The form of the electron–phonon cooling has been predicted for the low temperature limit, for a clean graphene system (with little diffusive scattering). Those predictions [38, 39] and measurements [16, 21] follow

$$P_{\rm eph} = \Sigma A\left(T^4 - T_0^4\right), \tag{2.5}$$

where A is the device area and $p = 4$. The magnitude of Σ is set by fundamental constants and the graphene deformation potential, D [39]. This is related to the thermal conductance by

$$G = \frac{{\rm d}P}{{\rm d}T}. \tag{2.6}$$

The form of electron–phonon scattering in (2.5) assumes small disorder (the electron mean-free-path $\ell_{\rm mfp}$ is long). Theoretical predictions which take disorder into account find a different form of the thermal conductance for very low [40] and high [41] temperatures for samples which have short $\ell_{\rm mfp}$. At low temperatures, the electron–phonon coupling is stronger and follows a $P_{\rm eph} \propto (T^3 - T_0^3)$ form, with a crossover temperature T_x given approximately by 60 K nm/$\ell_{\rm mfp}$. Typical mobilities and carrier densities of graphene on silicon dioxide

Table 1. Measurements of deformation potential determined through JNT. The column temperature denotes the range over which temperature measurements were conducted. The assumed form of the electron–phonon conductance differs in many of these studies based on the amount of disorder present [40, 41] and is denoted by p. A value of $p = 4$ assumes the clean limit of electron phonon coupling, while a value of $p = 3$ assumes a cooling power which is enhanced by disorder. For Betz *et al* the disorder is assumed to introduce supercollision cooling at high T, while for Fong *et al*, the disorder assisted cooling results in an enhancement of low T thermal conductance [40].

Study	T (K)	Σ (mW m^{-2} K^{-p})	p	A (μm^2)	R (k Ohm)	Substrate	D (eV)
Betz *et al* [44]	40–700	1200	3	6.2	1–3	BN	70
Betz *et al* [21]	4.2–400	0.5	4	13	2.8	BN	2
	4.2–400	2.0	4	6	1.3	BN	4
Fong *et al* [16]	2–30	70	4	102	30	Si/SiO_2	33
Fong *et al* [17]	0.3–30	200	3	102	10	Si/SiO_2	19
	0.3–30	300	3	55	5	Si/SiO_2	23
	0.3–30	1400	3	25	1.5	Si/SiO_2	51
This study	0.1–60[a]	30	4	1000	0.1	Si/SiO_2	11.5

[a] The temperature range over which D is determined is between 0.1 and 20 K.

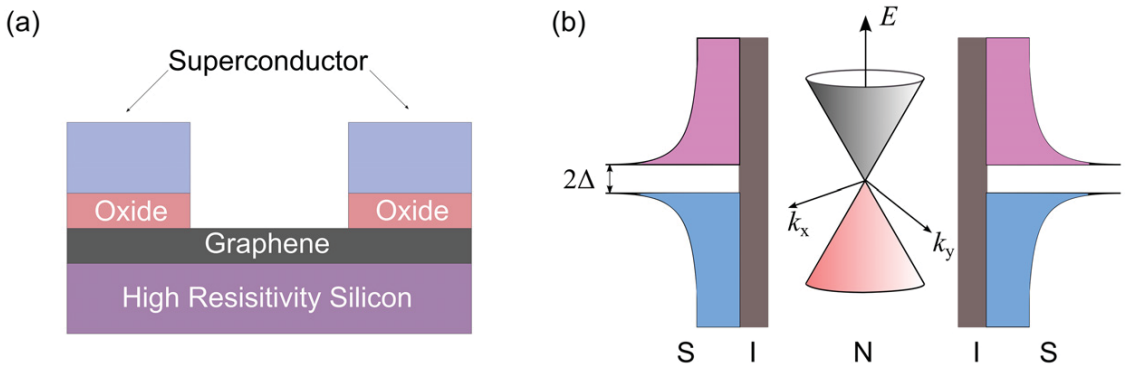

Figure 2. Schematic of a Superconductor-Insulator-Graphene-Insulator-Superconductor (SINIS) device (*a*) and band structure of graphene sandwiched by SIN contacts (*b*). The hot electrons in graphene (N) are confined by the SC tunnel junctions, minimizing $G_{\rm diff}$. The tunnel barriers are formed using metal oxide thin films.

(SiO_2) give $T_x \sim 1$ K This power law dependence at low temperatures has been observed in, to the authors' knowledge, one study of the thermal behaviour of graphene [17], which measured devices on an SiO_2 substrate. However, the authors of that study observed a T^2 dependence of the resulting $G_{\rm eph}$ at temperatures much higher than T_x. Use of either a boron nitride (BN) substrate or suspending the graphene has been shown to yield very high graphene mobilities [42, 43]. Either of these two approaches would increase $\ell_{\rm mfp}$ so that T_x would be below 0.1 K and the T^4 behaviour of (2.5) would extend down to 0.1 K. As it is possible to reduce T_x below temperatures considered in this study, $T \sim 0.1$ K, we use (2.5) to predict the device behaviour.

Our calculations for single-photon detection find an upper limit on Σ that will allow for detection of single THz photons using JNT. We find this upper limit to be $\Sigma_{\rm max} \approx 5\,{\rm mW\,m^{-2}\,K^{-4}}$. For $\Sigma > \Sigma_{\rm max}$, we find $\delta T \geqslant \Delta T_{\rm avg}$, where $\Delta T_{\rm avg}$ is the average temperature increase measured over τ:

$$\Delta T_{\rm avg} = \frac{1}{\tau}\int_0^{\tau} (T(t) - T_0)\,{\rm d}t. \tag{2.7}$$

For $\delta T \geqslant \Delta T_{\rm avg}$, one cannot clearly distinguish many real photon absorption events from the apparent fluctuations of the baseline temperature (with no absorbed photons). The physical problem is that the thermal relaxation time is too short, resulting in large values of $\delta T_{\rm readout}$ in the temperature readout, as given by (2.3).

An experimental value of $\Sigma < \Sigma_{\rm max}$ has been reported in only one study [21]. Those data were taken at $T > 4$ K. That small reported value of Σ indicated initial promise for implementation of a graphene single photon detector. All recent studies of the graphene thermal conductance have reported values of Σ that are considerably larger than $5\,{\rm mW\,m^{-2}\,K^{-4}}$ [16, 17, 44] (see table 1) and many of these measurements extend into the relevant temperature range below 4 K. These values of Σ are too large to allow for detection of single THz photons. However, we show in section 4.1 that even for a value of Σ larger than $\Sigma_{\rm max}$, graphene can be an effective power detector.

2.2. Resistive tunnel-junction thermometry

Direct resistive thermometry may be realized in graphene-superconductor tunnel junctions (SINIS, schematics shown in figure 2), whose tunnelling conductance at $|V| \ll k_{\rm B}T$ has a strong dependence on the electron temperature [28]:

$$R_{\rm c}(T) = R_0 \exp(\Delta/k_{\rm B}T) \tag{2.8}$$

for an ideal tunnel junction. At low temperatures $k_{\rm B}T \ll \Delta$ and with a voltage bias $V \ll \Delta/e$, the junction resistance

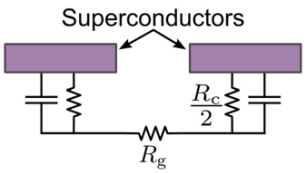

Figure 3. Circuit model of a SINIS device. The SC leads are coupled to graphene both resistively and capacitively, in parallel. Because the device is fabricated on high resistivity silicon and cooled to low temperatures, there are no free charge carriers in the substrate and capacitance across the graphene channel is negligible.

is large (∼MΩ) due to the suppression of quasiparticle tunnelling. This also provides the mechanism of hot electron confinement. In practice, the graphene absorber would be coupled to an antenna with an impedance typically on the order of 100 Ω. The tunnel junctions have been shown to behave capacitively at high frequencies [45] so the large junction resistance is shorted out at THz, as shown in the lumped parameter model of the contacts in figure 3. If an oxide with a sufficiently high dielectric constant is used as the tunnel barrier, the high frequency impedance of the tunnel junctions is negligibly small and the total device impedance is dominated by the resistance of graphene: $R_g = \rho_s L/W$; ρ_s is the sheet resistance, L is the length, and W is the width of the conducting channel. With a proper choice of aspect ratio for the graphene, the device impedance can match that of the antenna, allowing for high coupling efficiency. However, at lower frequencies, the device has total resistance $R(T) = R_c(T) + R_g$ which is much greater than 100 Ω and can confine the heated electrons.

To measure its resistance at low frequencies, a SINIS device may be either current- or voltage-biased. Here we will limit our discussion to voltage biasing. With no absorbed photons, a voltage-based device would have very small background 'dark current' because of the large junction resistance. This small background signal allows the current amplifier to operate at maximum sensitivity for photon power detection.

The dc bias voltage is chosen to optimize the current response. This has several requirements. The device needs to be biased at $V_c \ll \Delta/e$, with V_c the voltage across each tunnel junction, to ensure a strong dependence of R on temperature, and also to achieve thermal confinement. Additionally, Joule heating due to the bias voltage should be negligibly small. For voltage-biasing, when the device resistance decreases with increasing temperature, the Joule power dissipation increases. This positive electro-thermal feedback may lead to thermal runaway if the Joule heating were too large. Finally, the bias voltage should be large enough that the change of the current ($I = V/R$) is maximized and measurable within the sensitivity of a practical current amplifier. These criteria place strong limitations to the choice of the device parameters including the gap energy of the superconductor Δ and the normal-state junction resistance R_0.

2.3. Detector sensitivity: power detection

The power detection sensitivity of a bolometer is described by its noise equivalent power (NEP). The NEP is the power incident on the bolometer such that the signal-to-noise ratio is 1 in a 1 Hz post-detector bandwidth. We seek to determine what is important for minimizing the NEP for this detector. The rms intrinsic fluctuations that give rise to equation (2.2) also set a limit on the NEP,

$$\mathrm{NEP}_{\mathrm{intr}} = \sqrt{4k_B T^2 G}, \tag{2.9}$$

which is optimized by minimizing G.

For the SINIS configuration with resistive readout, we consider two major cooling channels: $G = G_{\mathrm{diff}} + G_{\mathrm{eph}}$ (Because this device can read out at low frequencies (< MHz), the design can suppress the contribution of G_{photon}). The diffusion thermal conductance is determined by the SIN contact resistance, since it is much greater than the graphene sheet resistance. G_{diff} is given by the Wiedemann–Franz law: $G_{\mathrm{diff}} = \alpha \mathcal{L} T/R$, where α is a geometrical factor (in the case of the SINIS structure, $\alpha = 4$ for $R \approx R_c$) and $\mathcal{L} = 2.44 \times 10^{-8}\,\mathrm{W\,\Omega\,K^{-2}}$ is the Lorentz number [34]. For the electron–phonon thermal conductance, we assume the low temperature, clean limit thermal conductance from acoustic phonons given by (2.5). In an optimized design, we must ensure that the phonon thermal conductance is sufficiently small to minimize the intrinsic NEP.

As with the Johnson noise readout, the amplification system used to measure the device response also places a limit on the device performance. Because the device is voltage biased, the response due to photon radiation can be characterized by its current responsivity, $\mathcal{R} = I_{\mathrm{avg}}/P_\gamma$, where P_γ is the incident photon power and I_{avg} is the resulting average change of current. This response then needs to be compared to the noise properties of the readout system. The noise of a field-effect transistor (FET) amplifier can be expressed as a current spectral density S_I with units of $\mathrm{A\,Hz^{-1/2}}$. The total readout NEP is then given by the ratio of the current noise divided by the device's current responsivity:

$$\mathrm{NEP}_{\mathrm{readout}} = S_I/\mathcal{R}. \tag{2.10}$$

Due to the highly non-linear nature of $R(T)$ in a SINIS device, direct estimation of its performance under photon radiation is not straightforward. Here we set up a time-dependent thermal equation, which can be solved numerically to determine I_{avg}. Due to the large electron–electron scattering rate, upon absorbing a photon with energy $E = h\nu$, the electrons in graphene quickly equilibrate within themselves at an elevated temperature T_i. The temperature of the electron gas then starts to equilibrate with the environment through power dissipation:

$$\gamma A \frac{\mathrm{d}T}{\mathrm{d}t} = -\Sigma A \left(T^4 - T_0^4\right) - \frac{\alpha \mathcal{L}}{2R}\left(T^2 - T_0^2\right) + \frac{V^2}{R}. \tag{2.11}$$

The three terms on the right side of the equation correspond to phonon cooling, diffusion cooling, and Joule heating under a voltage bias. This equation treats the limiting case where the temperature is uniform in the graphene. That applies for the SIN and SN detector geometries, where hot electrons are unable to diffuse out the leads. The total device resistance is given by $R = R_c + R_g \approx R_c$ in the intended range of operation. R decreases sharply upon absorbing a single photon, then rises

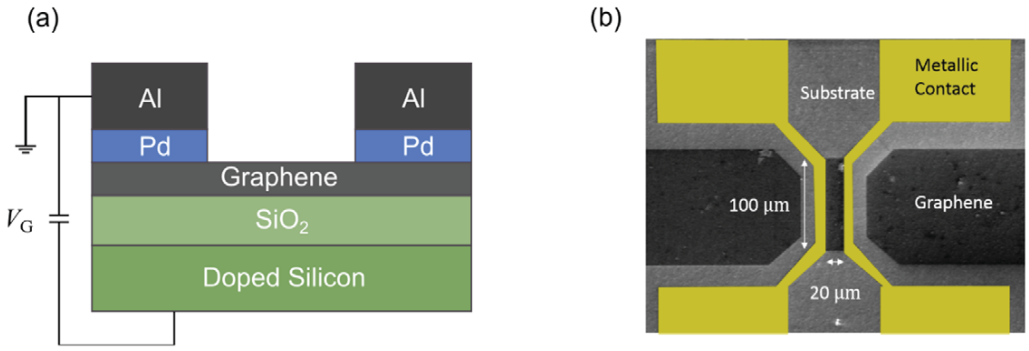

Figure 4. Schematic of measured SN device (*a*) and image of a typical graphene device (*b*). The SN device is produced on a doped silicon substrate (700 μm thick), with a 290 nm thick SiO_2 layer. The Pd/Al contacts are 5 nm and 50 nm thick, respectively. The graphene devices all had channel widths of $W = 100\,\mu$m and channel lengths L of 10, 20, 100, or 200 μm. The substrate is evident next to the metal contact film because the graphene was etched away to precisely define the device area.

back over a period of time depending on the dynamics of the energy dissipation. Consequently, with each photon absorbed the current through the device sharply increases and then decreases back to near-zero value at the base temperature. This is plotted below in figure 9 for specific favourable parameters which are given in section 4.3. We consider a photon incoming rate which is low enough so that there are only single photon events. Over a time period of τ, the average current measured at a fixed bias of V is:

$$I_{\text{avg}} = \frac{1}{\tau}\int_0^\tau I\,(t)\,\mathrm{d}t = \frac{1}{\tau}\int_0^\tau \frac{V}{R_0}\exp\left[-\frac{\Delta}{k_{\text{B}}T}\right]\mathrm{d}t. \qquad (2.12)$$

For the device to operate effectively as a power detector, the device parameters used in the equations above should be chosen so that the average current I_{avg} is measurable and varies significantly with the input power. Since $R(T)$ is strongly non-linear, the current response of the SINIS detector is not linear in photon energy. However, for low count rates at a given photon energy, the current response is linear in photon power. Much as with the Johnson noise readout method, the magnitude of Σ in (2.5), directly impacts the performance of this detector. Because of significant variation in reported values of Σ, we have conducted measurements of thermal conductivity of graphene systems to more accurately assess graphene's potential as a detector of THz photons, and present these measurements in the following section.

3. Graphene thermal conductance

In order to obtain a better understanding of the electron–phonon process in graphene, we performed steady-state heating measurements on graphene systems. Through these studies of graphene thermal behaviour using JNT, we were able to extract a value for Σ allowing for greater precision and confidence when predicting device performance.

3.1. Experimental design

The samples we discuss in this section were prepared from commercial (ACS-Material) graphene produced by chemical vapour deposition (CVD). Graphene produced through CVD rather than exfoliation was used so that the devices could have a precisely defined area, and could be fabricated to have dimensions of order 100s of microns. The graphene comes on a heavily doped, oxidized silicon substrate with a 290 nm-thick SiO_2 layer. Our devices are fabricated in a multistep process. First, we pattern the graphene with electron-beam lithography and then conduct an oxygen etch which defines the device area. Each of the graphene devices had a channel width of $W = 100\,\mu$m and a channel length L which ranged from 10–200 μm. The large device dimensions served two primary purposes. First, the large channel width reduced the total contact resistance, and by measuring devices of different lengths, we determined that the contact resistance was negligible for the studied devices. Additionally, the large total area of the graphene device maximized the contribution of the electron–phonon total conductance to G, as $G_{\text{eph}} \propto$ Area Thus, even if the contacts did not confine the heated electrons, G_{eph} would still have a substantial contribution to G above 5 K as G_{diff} depends only on the electrical resistance, not area.

Next, an additional electron-beam lithography step is performed to define the contacts. The graphene is metallized either with palladium/aluminium (Pd/Al) or titanium/palladium/niobium nitride (Ti/Pd/NbN) contacts (schematic shown in figure 4). With both Al and NbN contacts [44, 45], indications of Andreev reflection had previously been observed. This suggests that these SC leads can provide effective thermal confinement well below their critical temperature. In our experiments measuring the thermal properties reported here, we did not see significant thermal confinement by the SC contacts (We did not work to optimize the metallurgy to achieve the thermal confinement).

The samples are mounted on a circuit board containing a bias-tee. This allows for simultaneous dc bias and microwave measurements. This sample stage is bolted onto the mixing chamber of a cryogen-free dilution refrigerator and is cooled to below 50 mK. We perform measurements at an elevated base temperature of $T_0 = 100$–400 mK by locally heating the stage. This ensures that the graphene's base electron temperature is approximately equal to the bath temperature of 100–400 mK as measured by a ruthenium oxide thermometer on the stage. RC filters at the 4 K stage, and a printed circuit board filter [46], sandwiched by Eccosorb [47], at the

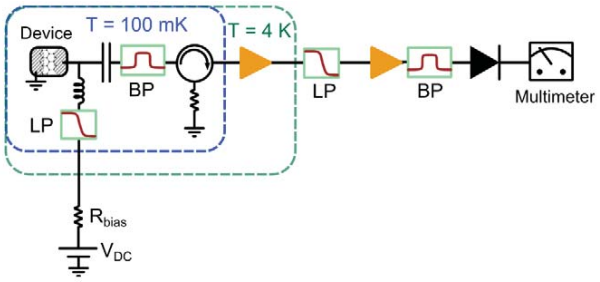

Figure 5. Schematic of the measurement setup. The hatched regions of the device represent the SC leads. LP and BP indicate microwave low-pass and band-pass filters, respectively. The capacitor and inductor at the 100 mK stage represent the bias-T.

mixing chamber temperature are used to reduce electrical noise incident on the sample from the external environment.

To characterize the thermal conductance, we heat the graphene sample using a dc current. The sample length is much longer than the electron–electron inelastic scattering length [26], so the electron system has a well-defined temperature distribution $T(x)$. Thus, the resistive graphene sheet is in the interacting hot-electron regime [48]. The heated electrons emit 1D blackbody radiation, (2.1) in the low frequency limit, corresponding to the average electron temperature $\tilde{T}$ This noise signal is amplified by a cryogenic low-noise amplifier and passed through a microwave band-pass filter centred at 1.3 GHz ($k_B T/h = 2$ GHz at $T = 100$ mK). The amplified signal is rectified by a Schottky diode, whose output is a voltage change proportional to the incident microwave power change (experimental schematic shown in figure 5). The change in diode output voltage due to applying a dc current to the device is thus proportional to the change in the average temperature of the electron system so that $\Delta V_{\rm diode} = \kappa \Delta \tilde{T}$.

The thermal conductance can then be calculated by taking the derivative of the applied dc Joule power P with respect to the electron temperature. To determine the electron temperature of the graphene, we measure the output voltage of the diode power detector. To precisely determine the factor κ, we have developed a calibration procedure that avoids contribution from the free charge carriers in the substrate. These substrate electrons emit additional, unwanted microwave power when heated. This couples capacitively into the microwave system transmission lines. We have carefully developed a new calibration method using Joule heating of only the device.

In order to calibrate the device, we need to know the correspondence between current in the device and its electron temperature. To that end, we take two traces of the ac diode output voltage using a small, constant on-off (ac) Joule input power dissipated in the sample. One trace is taken as a function of the sample dc current, $I_{\rm sample}$, with the sample stage at its base temperature, T_0 (e.g. 100 mK). The second trace is taken as a function of the temperature of the sample stage, $T_{\rm stage}$, with $I_{\rm sample} = 0$. In both cases the ac component of the diode output is caused only by changes of the sample's temperature due to the imposed on-off (ac) power. This is because the

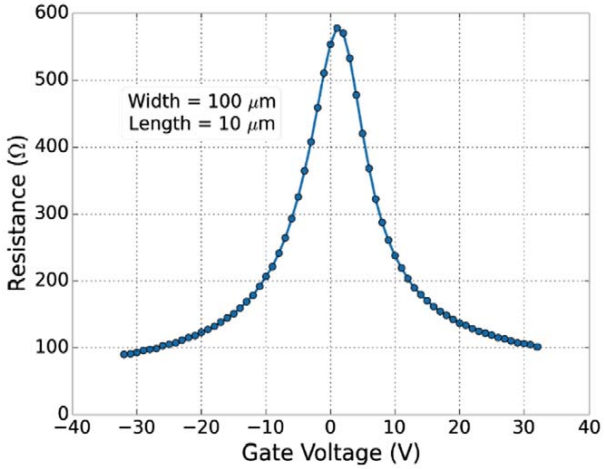

Figure 6. Measurement of device resistance as a function of gate voltage V_G. The charge neutrality point (peak in device resistance) is located at approximately $V_G = 2$ V.

substrate temperature and substrate microwave emission are not significantly affected by the power dissipated in the sample. We match the ac signals of the same value at $I_{\rm sample}$ and at $T_{\rm stage}$, and we thus calibrate the sample temperature T to $I_{\rm sample}$ In future experiments it would be desirable to have an insulating substrate to more easily avoid contributions from free charge carriers in the substrate. In that case, the calibration procedure would be simpler as the measurement would not have contributions from substrate microwave emission. Due to the large capacitance between contact pads and the substrate, a more standard calibration method (e.g. a measurement of $V_{\rm diode}$ as a function of T_0) can lead to errors in measured electron temperature of over a factor of 2.

We measure the electron temperature as a function of the dc power for a device which is 100 μm wide by 10 μm long with Pd/Al leads. The Pd and Al were 5 nm and 50 nm thick, respectively. This geometry gives a resistance of 90 Ω at a gate voltage of −32 V (see figure 6). Thus, the device is reasonably well-matched to the 50 Ω microwave output line and amplifier, without the need for a matching circuit. This contrasts to most other recent measurements of the electron–phonon coupling [16, 17, 21, 36]. Those measurements treated samples with lower electron density or less favourable graphene geometries (larger L/W ratio), both of which resulted in graphene with a higher electrical resistance. They either used a resonant coupling circuit to reduce the sample's impedance or had a substantial impedance mismatch, resulting in a large power loss of the microwave emission. Our approach with a sample resistance of order 50 Ω avoids those complexities.

3.2. Determination of Σ

The form of G given in (2.6) assumes that T is uniform across the graphene sample. Due to finite diffusion cooling, this is not the case for the samples we have measured. In order to interpret the cooling mechanisms that describe the dependence of the temperature on the dc bias current, we consider the

one-dimensional heat diffusion equation, assuming that heat transport is controlled predominantly by electron diffusion and phonon emission:

$$I^2 r = p_{\rm eph} - \frac{\partial}{\partial x}\left(g\,(x)\,\frac{\partial T(x)}{\partial x}\right). \tag{3.1}$$

I is the current passed through the sample, r is the electrical resistance per unit length, $T(x)$ is the position-dependent electron temperature, $g\,(x) = \mathcal{L}T(x)/r$ is the thermal conductivity given by the Wiedemann–Franz law [34], and $p_{\rm eph}$ is the electron–phonon cooling power per unit length, which is a function of $T(x)$ and T_0. The boundary conditions on this equation are defined by the thermal coupling between the graphene electron system and the metal leads. This coupling can be limited either by contact resistance for non-SC contacts or by confinement due to Andreev reflection or SC tunnel contacts. By measuring the dc properties of multiple graphene samples with different length-to-width ratios, we found that our devices did not have substantial contact resistance. We also did not observe thermal confinement due to Andreev reflection. Thus, the relatively massive leads impose a temperature $T(x) = T_0$ at each end of the graphene sample. Indeed, at low temperatures, the thermal conductance was consistent with cooling from out-diffusion into non-SC contacts [34, 49] (The Al films have $T_{\rm c} \approx 1.2$ K). Without confinement, the thermal conductance at 1 K due to out-diffusion $G_{\rm diff}$ is more than an order of magnitude greater than the thermal conductance due to electron–phonon coupling. Thus, our measurements at a heated temperature $T > 1$ K are the most informative. To solve the differential equation for $T(x)$, it was necessary to assume a form for the electron–phonon cooling power. We considered two regimes separately. In the low-temperature regime the cooling power is given in the clean limit by [39]

$$p_{\rm eph} = \Sigma W\left(T(x)^4 - T_0^4\right), \quad \text{for} \quad T \ll T_{\rm BG}, \tag{3.2}$$

where $T_{\rm BG}$ is the Block-Gruneisen temperature which depends on carrier density and W is the device width. For our sample and its carrier density $n \approx 2.4 \times 10^{12}\,{\rm cm}^{-2}$, $T_{\rm BG} \approx 85$ K. The prefactor Σ has been predicted to have the form

$$\Sigma = \frac{\pi^2 D^2\,|E_{\rm F}|\,k_{\rm B}^4}{15\rho_{\rm M}\hbar^5 v_{\rm F}^3 s^3}. \tag{3.3}$$

In this expression, $E_{\rm F} = \hbar v_{\rm F}\sqrt{\pi n}$ is the Fermi energy, $\rho_{\rm M} = 7.6 \times 10^7\,{\rm kg\,m}^{-2}$ is the mass density of graphene, $v_{\rm F} = 10^6\,{\rm m\,s}^{-1}$ is the Fermi velocity and $s = 2 \times 10^4\,{\rm m\,s}^{-1}$ is the speed of sound in graphene. In the high-temperature limit, supercollisions [41] are expected to enhance the thermal conductivity of the system, with total cooling power:

$$p_{\rm eph} = W\left[h\,(T(x) - T_0) + J\left(T(x)^3 - T_0^3\right)\right], \quad \text{for} \quad T \gg T_{\rm BG}, \tag{3.4}$$

where

$$h = \frac{D^2 E_{\rm F}^4 k_{\rm B}}{2\pi\rho_{\rm M}\hbar^5 v_{\rm F}^6} \quad \text{and} \quad J = \frac{2\zeta(3) D^2\,|E_{\rm F}|\,k_{\rm B}^3}{\pi^2\rho_M\hbar^4 v_{\rm F}^3 s^2 \ell_{\rm mfp}}. \tag{3.5}$$

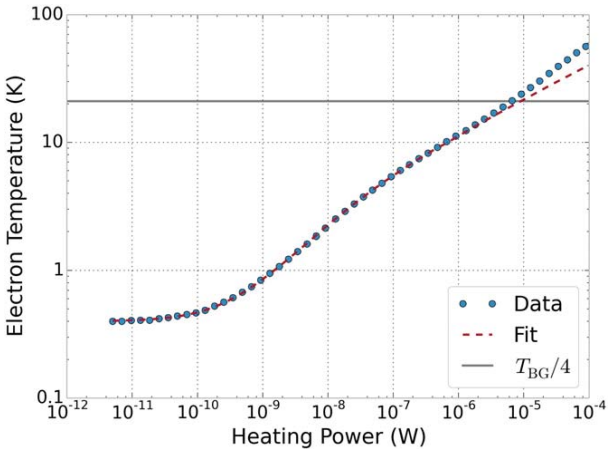

Figure 7. Average electron temperature $\bar{T}$ as a function of dc Joule heating power, calculated from device resistance R and diode coupling κ. The dashed line is a calculation of $\bar{T}$ from (3.1), with $p_{\rm eph}$ given by (3.2), using the device resistance, heating power, and a deformation potential of $D = 11.5$ eV. Numerical calculations [39] demonstrate that the predicted cross-over between the low- and high-temperature limits occurs at approximately $T_{\rm BG}/4$. For the carrier densities in this measurement, $T_{\rm BG} \approx 85$ K, and $T_{\rm BG}/4$ is denoted by the solid horizontal line.

We solved this differential equation for $T(x)$ and integrated over the length of the device to obtain the average temperature $\bar{T}$. The expression for the electron temperature as a function of bias current in (3.1) for the low temperature regime is then optimized to fit the measured data. Only one free parameter, D, is used in this fit, which is plotted in figure 7. In the low temperature regime, the deformation potential was found from this fitting procedure to be $D = 11.5 \pm 1.0$ eV, falling within the typical range of measurements for D of 10–30 eV [39, 50]. The power dependence of the electron temperature in both the high (3.4) and low (3.2) temperature regimes should have different power law dependences, but the same value of D should apply. However, we found that, while the high temperature T^3 dependence was consistent with our measurements, the magnitude of the cooling power was much greater for our device than predicted by (3.4). This difference is similar to findings from other groups, which have measured a larger experimental magnitude of $p_{\rm eph}$ than predicted by the theory for supercollisions [4, 44, 51]. The magnitudes in these studies would agree if one had $D \gg 30$ eV. This value for D is substantially larger than what we deduce at lower temperatures.

In fitting the data, we disregard the dirty limit as our value for $\ell_{\rm mfp}$ is sufficiently large. We have $T_x \approx 1$ K for our sample and the form of electron–phonon cooling cannot be accurately measured below a few kelvin as $G_{\rm diff}$ becomes the dominant cooling mechanism.

The measured deformation potential at low temperatures used to fit (3.1) corresponds to $\Sigma = 30 \pm 5\,{\rm mW\,K}^{-4}$ at a gate voltage of -32 V ($n \approx 2.4 \times 10^{12}\,{\rm cm}^{-2}$). Note that $\Sigma \propto \sqrt{n}$ [39] so the carrier density is critical to understanding the physical implications of a quoted value for Σ. The small uncertainty in this result arises from systematic uncertainty in the microwave coupling measurement of around 5%. This result, and those of other groups are presented in table 1.

We find that our leads unfortunately do not confine the hot electrons at low temperatures where our device is below the critical temperature of the SC leads. The expected confinement, which was not observed, would manifest as a thermal conductance lower than what would be expected for unimpeded cooling of the device through hot electron out-diffusion. Due to the large value of L relative to $\ell_{\rm mfp}$ and the negligible contact resistance, other signatures of Andreev reflection (the enhancement of conductance or the presence of a supercurrent) [28] would not be present even if the contacts did prevent carrier out-diffusion. While the measurements presented here are for the Pd/Al devices, we note that we also do not see confinement in the Ti/Pd/NbN. While this finding of negligible heat confinement was unexpected, there are many processing steps involved in fabricating the devices which may suppress superconductivity in the leads where they contact the graphene. As the leads are deposited on post-transferred CVD graphene, there is residual polymer from the transfer process on the surface of the graphene that we are unable to remove before the deposition [52]. This thin surface residue may have a reaction with the deposited material, reducing its $T_{\rm c}$. Future investigations will need to consider transferring the graphene onto prelithographed contacts, or using exfoliated graphene to avoid the contamination associated with the transfer process.

The presence of out-diffusion cooling by the contacts prevents us from observing the form of the electron–phonon cooling below a few Kelvin. For our samples, which have $\ell_{\rm mfp} \approx 50\,{\rm nm}$, we would need to observe the electron–phonon behaviour below 1 K in order to establish whether scattering in the presence of disorder plays a role in the cooling process. However, because there are proven techniques to achieve reduced disorder in graphene [42, 53], our result is still important for predicting device performance at temperatures below 1 K for those realizable devices with $T_x < 0.1\,{\rm K}$.

4. Predicted device performance

The graphene devices measured in this study were fabricated with areas optimized for the measurement of Σ and are too large for effectively detecting THz photons, so antennas were not lithographed on the device. Additionally, the failure of the present SC contacts to confine the hot electrons in the graphene precludes sensitive detector operation and testing at the temperatures of interest $T_0 \approx 0.1\,{\rm K}$. For the implementation of an actual detector, it will be critical to suppress the out-diffusion of hot electrons through the leads; otherwise, $G_{\rm diff}$ will be too large and the device will have poor sensitivity. However, we can predict the performance of a graphene-based THz photon detector assuming adequate confinement of the hot carriers by the SC contacts, using the value for D we have determined experimentally. We address the cases of Johnson noise readout and resistive readout of the SINIS structure separately, considering both single photon and bolometric power detection using JNT, and focusing only on bolometric power detection with the resistive measurement. For the SINIS structure, the large value of R means that the electrical RC time is too long compared to τ to record individual single-photon events.

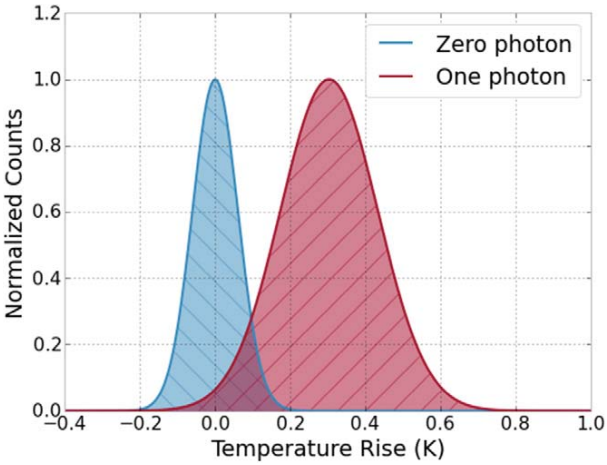

Figure 8. Predicted histogram of the measured temperature rise for an ensemble of single photon detection events. The calculations are based on a bath temperature of 100 mK, a heat capacity of $C = 4 \times 10^{-22}\,{\rm J\,K^{-1}}$, an electron–phonon coupling of $\Sigma = 19\,{\rm mw\,K^{-4}\,m^{-2}}$ (corresponding to $n = 10^{12}\,{\rm cm^{-2}}$ with $D = 11.5\,{\rm eV}$), and a 1 THz photon energy $E = 7 \times 10^{-22}\,{\rm J\,K^{-1}}$. The heat capacity corresponds to a graphene area of about 6 $\mu{\rm m}^2$ at a carrier density of $n = 10^{12}\,{\rm cm^{-2}}$. The temperature rise is the average value of the measured temperature increase over the time measurement window τ. With no noise, this is predicted to be $\Delta T_{\rm avg} \approx 300\,{\rm mK}$ after absorption of a single THz photon. The zero photon 'events' are samples of the baseline with no photons; their histogram is narrower because $T = T_0 = 100\,{\rm mK}$, so the equilibrium noise equations apply. The value of C was chosen to minimize the overlap of the two distributions.

4.1. Johnson noise readout: single-photon detection

We can predict the performance of this device for single-photon detection by considering its capacity to distinguish between zero-photon (baseline) and one-photon events. We consider a base temperature of $T_0 = 100\,{\rm mK}$. A higher base temperature would give degraded performance and a much lower base temperature would give only a small improvement in sensitivity while significantly limiting count rate due to the much slower decay of ΔT. For our measured value of Σ and an optimized $C_0 = 4 \times 10^{-22}\,{\rm J\,K^{-1}}$ (chosen to maximize $\Delta T_{\rm avg}/\delta T$) the temperature rise pulse has a typical decay time of $\tau = 0.1\,\mu{\rm s}$ [11]. In figure 8, we plot our prediction for normalized histograms of the number of counts from zero- and one-photon events against the measured average temperature rise $\Delta T_{\rm avg}$. We consider a large ensemble of individual single-photon absorption events.

The zero-photon events sample the baseline and baseline temperature fluctuations with no photons absorbed. Ideally, with very small noise, these histograms would be well-separated. In that case, we could define a threshold temperature rise to distinguish single-photon events from zero photon events (the baseline samples) In the absence of any noise, the average temperature rise is $\Delta T_{\rm avg} = 0.3\,{\rm K}$. However, the measured pulses will have a range of temperature rises for individual pulses due to intrinsic and readout fluctuations. The readout noise is calculated assuming a near-quantum-limited amplifier [54], with $T_{\rm A} = 150\,{\rm mK}$, $B = 150\,{\rm MHz}$, and centre frequency $f_0 = 1\,{\rm GHz}$ [11]. While this amplifier has

not been developed, the noise is approximately six times the quantum limit, $T_{QL} = hf_0/2k_B$, and similar performance has been achieved at a higher centre frequency $f_0 = 10$ GHz [55]. For the value of D measured, these histograms show substantial overlap; a graphene device with this deformation potential would not be an effective single photon counter for 1 THz photons.

The majority of the literature reports values of D that are at least as large as we found in our measurements. This suggests that the outlook for using graphene with a JNT readout to detect single THz photons is not promising unless graphene can be prepared with smaller values of D. We do find that a graphene device would have promise as a THz power detector if different device operating parameters were employed, even with the measured value $D = 11.5$ eV. We discuss this in the following section.

4.2. Johnson noise readout: power detection

For bolometric power detection, a larger device area can be used as we are no longer constrained to have a small C_0 to detect individual THz photons. A larger area of graphene is preferred so that there is a linear response to an incident power flux. Consider a large area of graphene, approximately 400 μm^2, cooled to 50 mK, with a carrier density of $n \approx 10^{12}$ cm^{-2}. For a sample this large, the response will be nearly linear following the absorption of a THz photon. We can then use the near-equilibrium predictions of the device sensitivity.

Assuming the clean-limit form of electron–phonon thermal conductance given by (2.5) and that the electron heat is confined to the graphene by SC contacts, we find a thermal conductance of $G_{eph} \approx 4 \times 10^{-15}$ W K^{-1}. With this value of thermal conductance, the cooling of the graphene device after photon absorption can be modelled [11], yielding $\tau \approx 2.5\,\mu$s. As the arrival rate for photons in the proposed applications does not exceed 10^5 s^{-1}, and $\tau \approx 2.5\,\mu$s, the photons will be sufficiently separated in time to avoid overheating of the device. Using (2.9) to calculate the equilibrium fluctuations and (2.3) to calculate the apparent temperature fluctuations due to the readout, we can estimate that the readout noise dominates and sets a total NEP $\approx 4 \times 10^{-19}$ W Hz$^{-1/2}$, assuming a Johnson noise readout bandwidth of 10 MHz. This 10 MHz readout bandwidth allows for many devices to be read out with one amplifier having a 1 GHz centre frequency. We believe that 10s of devices, up to perhaps 50 to 100 could be multiplexed in this fashion [12]. This NEP is competitive with current state-of-the-art detectors [18].

The benefits of using this readout approach must carefully be balanced with the instrumentation and fabrication limitations when considering this system in an observatory instrument. By using a larger readout bandwidth, the device noise can be further improved as NEP $\propto 1/\sqrt{B}$ for NEP $\geqslant 10^{-19}$ W Hz$^{-1/2}$, but this comes at the expense of having to dedicate a larger bandwidth for each readout channel. In a large system, it would be desirable to read out many channels simultaneously with one amplifier and each channel with a slightly different centre frequency. Using a small bandwidth per channel, such as 10 MHz, would more easily allow for multiplexing in the readout-frequency domain when using microwave frequencies centred at approximately 1 GHz.

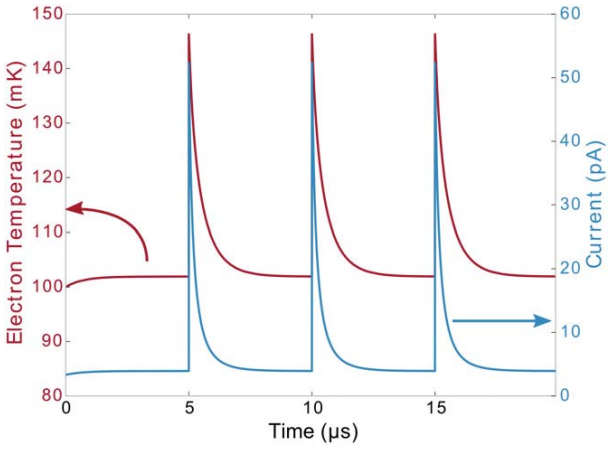

Figure 9. Simulation of the time evolution of electron temperature (red) and current (blue) with 1 T Hz photons arriving at a rate of 0.2 M Hz. The parameters used in the simulation are described in the main text. At $t = 0$, the electron temperature is chosen to be the bath temperature ($T_0 = 100$ mK). The initial small rise in electron temperature is due to Joule heating from the bias voltage.

4.3. Resistive readout: power detection

The performance of a SINIS bolometer with resistive readout can be simulated by numerically solving (2.10) with the measured value for Σ. We consider a device operating at the base temperature $T_0 = 0.1$ K and choose several parameters in the simulations: SC energy gap Δ, normal state total resistance R_0, dc bias voltage V, and graphene area A. With each set of parameters, we calculate the time response of the electron temperature and the current signal $I(t)$, and the average current upon absorbing photons. In figure 9, we show an example of the simulation. In this case, $A = 300\,\mu$m^2, $\Delta = 75\,\mu$eV, and $R_0 = 1\,$kΩ. The bias voltage across the SINIS device is 20 μV. Terahertz photons are absorbed at various incoming rates from 0.2–5 MHz. Under these conditions, current pulses with 50 pA peak amplitude are generated, corresponding to a peak electron temperature rise of 50 mK. The current pulse from a single 1 THz photon decays to the 'dark' background in less than 1 μ s. Detection of a single photon event appears to be beyond the capability of presently available low-noise amplifiers since a signal bandwidth > 1 MHz is required [56]. On the other hand, given a sufficiently long integration time, the average current signal is measurable, and the graphene device can operate as a highly sensitive power detector, as shown in figure 9. Here the average current changes roughly linearly from a 'dark' current of 5 to ≈60 pA with a photon rate of 5 MHz. The thermal conductance is dominated by electron–phonon cooling, and thus the intrinsic NEP of this device is estimated to be NEP$_{intr} = 2 \times 10^{-19}$ W Hz$^{-1/2}$.

We next consider the contribution of amplifier noise to the total NEP. First we calculate the current responsivity in A/W. At an absorption rate of 10^5 s^{-1}, 1 THz photons have

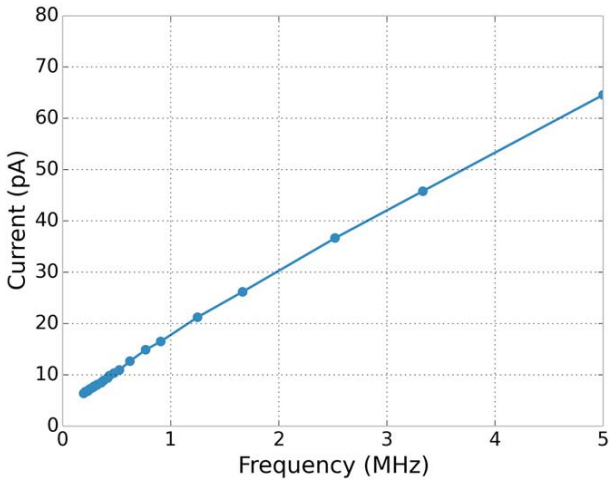

Figure 10. Simulation of the average current as a function of photon arrival rate. The extrapolation of the calculated data points shows a zero-signal current. The change of the average current from the zero-signal current can be used as a measure for the incident power.

a power of $P_\gamma = 7 \times 10^{-17}$ W. Using the initial slope of the current response in figure 10, we find a responsivity of $\mathcal{R} = 2 \times 10^4$ A W^{-1}. Low-noise FET voltage amplifiers have been produced with current noise at low frequencies (∼10–100 Hz) limited by the room-temperature input resistor (4 fA Hz$^{-1/2}$ for $R = 1$ GΩ). We consider finite audio readout frequencies to avoid $1/f$ FET noise, which requires a THz photon source chopped on/off at an audio frequency. Current amplifiers that operate directly in a cryogenic environment with extremely low current noise have been developed [57, 58]. Assuming that the noise in a current amplifier configuration with a cryogenic feedback resistor can be ∼1 fA Hz$^{-1/2}$, the contribution of the amplifier current noise to the total NEP is NEP$_{\text{readout}} = 5 \times 10^{-20}$ fA Hz$^{-1/2}$. This is much less than the intrinsic NEP, so the amplifier noise will be neglected in the following discussion.

Finally, it is also necessary to consider the effects of shot noise across the tunnelling contacts [59]. For low transmissivity barriers, a dc current across the barrier generates a current noise in parallel to the device, equal to $I_N = \sqrt{2eI}$ at frequencies such that $eV \gg hf$. For the 5 pA dark current above, $I_N \approx 1$ fA Hz$^{-1/2}$, comparable to the amplifier current noise. However, given that audio amplifiers typically have an input impedance much larger than the device impedance, much of that noise current will be shunted to the device and not be amplified with the measured signal. Thus, shot noise will also not contribute substantially to the total device noise.

There are several technical challenges that must be overcome to realize this low NEP. First, the SC gap of the contacts is optimized at $\Delta \approx 75\,\mu$eV ($T_c \approx 0.44$ K), a value which is not realized with existing superconductors commonly used for SIN tunnel contacts. A much larger SC gap would result in a device resistance which is too large; the resulting current from photon radiation would be too small to observe. A much smaller SC gap, on the other hand, would not provide sufficient thermal confinement. The optimized SC gap may be obtained by means of gap engineering using a multilayer material or by applying a small magnetic field to suppress the intrinsic gap of a higher T_c material (e.g. aluminium).

The second challenge is the size of graphene, which optimizes at a few hundred square microns. A much smaller graphene device would result in an electron temperature rise so large that the resistance response becomes saturated, yielding poor power contrast. While large size graphene films are available through the CVD technique, their quality may be limited and hence the clean-limit assumption in G_{eph} discussed previously may not accurately describe the system behaviour. On the other hand, with the rapid development of large area graphene synthesis, this issue may be resolved in the near future.

Finally, it remains a challenge to realize the ideal tunnel barrier that is assumed in (2.7). While this was assumed in all of our simulations, achieving SC tunnel junctions of sufficiently high quality has not been demonstrated thus far. However, with further developments in device fabrication, we expect this goal to be achievable.

5. Conclusions

For both JNT using SC contacts and resistive thermometry using SC tunnel junction contacts, graphene has the potential to be a competitive ultrasensitive detector of THz photons. Our simulations show that the relatively strong electron–phonon coupling that we measure in graphene effectively precludes its use for single-photon detection in the THz range. However, by turning instead to power measurements, where a larger averaging time can allow for more sensitive measurements, graphene can achieve a very low NEP.

There remain fabrication challenges associated with both JNT devices using SN contacts and tunnelling devices with SIN contacts. There are specific advantages to using one detection method over the other. In both cases, contacts which provide thermal confinement of heated electrons while still allowing effective readout of the temperature are unproven, though we see no obvious physical limitations on this front. Very sensitive and, as of yet, undeveloped microwave amplifiers are necessary to make JNT an effective measurement tool, while the tunnelling resistive readout requires a SC contact material which may need tuning to realize the necessary parameters. Finally, because the JNT mode of operation uses microwave frequencies, a frequency domain multiplexing (FDM) scheme can be used, dramatically decreasing the hardware required to operate a large array of pixels. The low frequency readout of the tunnelling resistance likely makes the use of FDM impractical for SIN devices employing a resistive readout. Consideration of each of these factors will be necessary to determine the direction of future studies and potential use of graphene devices to serve as ultrasensitive THz photon detectors.

Acknowledgments

The work at Yale was supported by NSF Grant DMR-0907082, an IBM Faculty Grant, and by Yale University. Facilities use at Yale was supported by YINQE and NSF MRSEC DMR

1119826. XD and HV acknowledge support from AFOSR-YIP Award No. FA9550-10-1-0090.

References

[1] Xia F, Mueller T, Golizadeh-Mojarad R, Freitag M, Lin Y, Tsang J, Perebeinos V and Avouris P 2009 *Nano Lett.* 9 1039–44

[2] Kim M-H, Yan J, Suess R J, Murphy T E, Fuhrer M S and Drew H D 2013 *Phys. Rev. Lett.* **110** 247402

[3] Gabor N M, Song J C W, Ma Q, Nair N L, Taychatanapat T, Watanabe K, Taniguchi T, Levitov L S and Jarillo-Herrero P 2011 *Science* **334** 648–52

[4] Graham M W, Shi S-F, Ralph D C, Park J and McEuen P L 2012 *Nat. Phys.* **9** 103–8

[5] Mueller T, Xia F and Avouris P 2010 *Nat. Photonics* **4** 297–301

[6] Cai X *et al* 2014 *Nat. Nanotechnol.* **9** 814–9

[7] Yan J, Kim M-H, Elle J A, Sushkov A B, Jenkins G S, Milchberg H M, Fuhrer M S and Drew H D 2012 *Nat. Nanotechnol.* **7** 472–8

[8] Spirito D, Coquillat D, De Bonis S L, Lombardo A, Bruna M, Ferrari A C, Pellegrini V, Tredicucci A, Knap W and Vitiello M S 2014 *Appl. Phys. Lett.* **104** 061111

[9] Mittendorff M, Winnerl S, Kamann J, Eroms J, Weiss D, Schneider H and Helm M 2013 *Appl. Phys. Lett.* **103** 021113

[10] Vicarelli L, Vitiello M S, Coquillat D, Lombardo A, Ferrari A C, Knap W, Polini M, Pellegrini V and Tredicucci A 2012 *Nat. Mater.* **11** 865–71

[11] McKitterick C B, Prober D E and Karasik B S 2013 *J. Appl. Phys.* **113** 044512

[12] Karasik B S, McKitterick C B and Prober D E 2014 *Proc. SPIE* **9153** *Millimeter, Submillimeter, and Far-Infrared Detectors and Instrumentation for Astronomy VII* ed W S Holland and J Zmuidzinas (Bellingham, WA: International Society for Optics and Photonics) p 915309

[13] Karasik B S, McKitterick C B and Prober D E 2014 *J. Low Temp. Phys.* **176** 249–54

[14] Du X, Prober D E, Vora H and Mckitterick C B 2014 *Graphene 2D Mater.* **1** 1–22

[15] McKitterick C B, Vora H, Du X, Karasik B S and Prober D E 2014 *J. Low Temp. Phys.* **176** 291–8

[16] Fong K and Schwab K 2012 *Phys. Rev.* X **2** 031006

[17] Fong K C, Wollman E E, Ravi H, Chen W, Clerk A A, Shaw M D, Leduc H G and Schwab K C 2013 *Phys. Rev.* X **3** 041008

[18] Karasik B S, Sergeev A V, Prober D E and Sergeez A V 2011 *IEEE Trans. Terahertz Sci. Technol.* **1** 97–111

[19] Benford D J and Moseley S H 2004 *Nucl. Instrum. Methods Phys. Res.* A **520** 379–83

[20] Wallraff A, Schuster D I, Blais A, Frunzio L, Huang R-S, Majer J, Kumar S, Girvin S M and Schoelkopf R J 2004 *Nature* **431** 162–7

[21] Betz A *et al* 2012 *Phys. Rev. Lett.* **109** 056805

[22] Horng J *et al* 2011 *Phys. Rev.* B **83** 165113

[23] Nair R R, Blake P, Grigorenko A N, Novoselov K S, Booth T J, Stauber T, Peres N M R and Geim A K 2008 *Science* **320** 1308

[24] Santhanam P and Prober D 1984 *Phys. Rev.* B **29** 3733–6

[25] Altshuler B L, Aronov A G and Khmelnitsky D E 1982 *J. Phys. C: Solid State Phys.* **15** 7367–86

[26] Voutilainen J, Fay A, Häkkinen P, Viljas J, Heikkilä T and Hakonen P 2011 *Phys. Rev.* B **84** 045419

[27] Mather J C 1984 *Appl. Opt.* **23** 584

[28] Tinkham M 2004 *Introduction to Superconductivity* (New York: Dover)

[29] Beenakker C 2006 *Phys. Rev. Lett.* **97** 067007

[30] Borzenets I, Coskun U, Jones S and Finkelstein G 2011 *Phys. Rev. Lett.* **107** 137005

[31] Tarasov M A, Edelman V S, Mahashabde S and Kuzmin L S 2014 *IEEE Trans. Appl. Supercond.* **24** 1–5

[32] Efetov D and Kim P 2010 *Phys. Rev. Lett.* **105** 256805

[33] Richards P L 1994 Bolometers for infrared and millimeter waves *J. Appl. Phys.* **76** 1

[34] Kittel C 2004 *Introduction to Solid State Physics* (New York: Wiley)

[35] Dicke R H 1946 *Rev. Sci. Instrum.* **17** 268

[36] Karvonen J T, Taskinen L J and Maasilta I J 2004 *Phys. Status Solidi* **1** 2799–802

[37] Sergeev A V, Karasik B S, Gershenson M and Mitin V 2002 *Physica* B **316–317** 328–30

[38] Tse W-K and Das Sarma S 2009 *Phys. Rev.* B **79** 235406

[39] Viljas J K, Heikkilä T T and Heikkila T T 2010 *Phys. Rev.* B **81** 1–9

[40] Chen W and Clerk A 2012 *Phys. Rev.* B **86** 125443

[41] Song J C W, Reizer M Y and Levitov L S 2012 *Phys. Rev. Lett.* **109** 106602

[42] Du X, Skachko I, Barker A and Andrei E Y 2008 *Nat. Nanotechnol.* **3** 491–5

[43] Dean C R *et al* 2010 *Nat. Nanotechnol.* **5** 722–6

[44] Betz A C, Jhang S H, Pallecchi E, Ferreira R, Fève G, Berroir J-M and Plaçais B 2012 *Nat. Phys.* **9** 109–12

[45] Vora H, Nielsen B and Du X 2014 *J. Appl. Phys.* **115** 074505

[46] Mueller F, Schouten R N, Brauns M, Gang T, Lim W H, Lai N S, Dzurak A S, van der Wiel W G and Zwanenburg F A 2013 *Rev. Sci. Instrum.* **84** 044706

[47] Santavicca D F and Prober D E 2008 *Meas. Sci. Technol.* **19** 087001

[48] Steinbach A, Martinis J and Devoret M 1996 *Phys. Rev. Lett.* **76** 3806–9

[49] Prober D E 1993 *Appl. Phys. Lett.* **62** 2119

[50] Kubakaddi S 2009 *Phys. Rev.* B **79** 1–6

[51] Laitinen A, Oksanen M, Fay A, Cox D, Tomi M, Virtanen P and Hakonen P J 2014 *Nano Lett.* **14** 3009–13

[52] Liang X *et al* 2011 *ACS Nano* **5** 9144–53

[53] Wang L *et al* 2013 *Science* **342** 614–7

[54] Clerk A A, Devoret M H, Girvin S M, Marquardt F and Schoelkopf R J 2010 *Rev. Mod. Phys.* **82** 1155–208

[55] Ho Eom B, Day P K, LeDuc H G and Zmuidzinas J 2012 *Nat. Phys.* **8** 623–7

[56] Letzter S and Webster N 1970 Noise in amplifiers *IEEE Spectr.* **7** 67–75

[57] Schoelkopf R J, Wahlgren P, Kozhevnikov A A, Delsing P and Prober D E 1998 *Science* **280** 1238–42

[58] Prober D E 1974 *Rev. Sci. Instrum.* **45** 849

[59] Blanter Y M and Buttiker M 2000 *Phys. Rep.* **336** 1–166